MECHANICAL PROPERTIES OF a-CARBON INFILTRATED CARBON NANOTUBE TEMPLATED MATERIALS

by

Taylor S. Wood

Submitted to Brigham Young University in partial fulfillment

of graduation requirements for University Honors

Department of Physics and Astronomy

Brigham Young University

August 2011

Advisor: Robert Davis

Signature: _____

Honors Representative: Matthew Asplund

Signature: _____

ABSTRACT

MECHANICAL PROPERTIES OF a-CARBON INFILTRATED CARBON NANOTUBE TEMPLATED MATERIALS

Taylor S. Wood

Department of Physics and Astronomy

Bachelor of Science

Microdevices such as accelerometers and force sensors are changing the face of technology. Unfortunately, the type of material a device is made of considerably limits the extent of its practical applications and impedes microdevices from being used to their full potential. Carbon nanotubes (CNTs) contain many interesting physical properties and present an exciting material for use as a nanoframework to shape and reinforce the structure of microdevices. In this study, we use a method of growing, infiltrating, and characterizing carbon nanotube templated structures for use in microfabrication. Carbon nanotubes are first grown by Fe-catalyzed chemical vapor deposition after which infiltration of amorphous carbon (a-C) proceeds by chemical vapor deposition. a-C fills the spaces in between the CNTs, creating a CNT/nanotube composite material. Using cantilever structures fabricated from different Fe-catalyst thicknesses and different a-C infiltration times, we measure the extension vs. applied force of the cantilevers. We then

use this material to calculate the Young's modulus and yield stress of the nanocomposite. Young's modulus values for our material ranged from 1.67 – 7.87 GPa, depending on sample preparation conditions. Yield stress values of the composite material ranged from 53.7 – 147 MPa, depending on sample preparation conditions. Our results show that a thicker Fe-catalyst layer results in higher Young's modulus and yield stress values. Furthermore, our data indicate that the a-C infiltration time has little effect on the resultant materials properties of the nanocomposite. Our data characterize this material as a flexible material with moderate strength. We hope that with further optimization, it will soon be used in the fabrication of industrial devices.

ACKNOWLEDGEMENTS

I am sincerely appreciative of the assistance and guidance of my advisors, Dr. Robert C. Davis and Dr. Richard R. Vanfleet. Without their tutelage, this project would not have been possible. I would also like to thank Walter Fazio, Jason Lund, and Jun Song for their help in experimental fabrication and testing and Dr. Brian Jensen for his consultation and expertise. I am also grateful for research funding from the Brigham Young University Department of Physics and Astronomy and the Office of Research and Creative Activities. Finally, I would like to give special thanks to my parents, Dr. Steven G. Wood and Dr. Lorraine W. Wood, for their assistance in writing this thesis and for their constant support and encouragement throughout my schooling.

TABLE OF CONTENTS

LIST OF FIGURES

LIST OF FIGURES

LIST OF TABLES

Chapter 1

Introduction

1.1 Microdevices

In a lecture entitled "There is Plenty of Room at the Bottom," Richard Feynman speculated on the great potential of using nanosized devices and electronics as parts of larger machines[1]. Although his ideas were considered visionary at the time, nanoscale engineering of microdevices has recently become an increasingly viable and important branch of nanotechnology.

Microdevices are small electrical or mechanical devices built on the scale of micrometers (see Figure 1.1). They have great potential for real-world applications and are currently used as integral components of devices such as accelerometers, pressure sensors, and humidity sensors. Currently, most microdevices are made of silicon; however, many materials can be used. As we explore alternative materials for microdevice fabrication, we find limits that prevent them from being used to the fullest

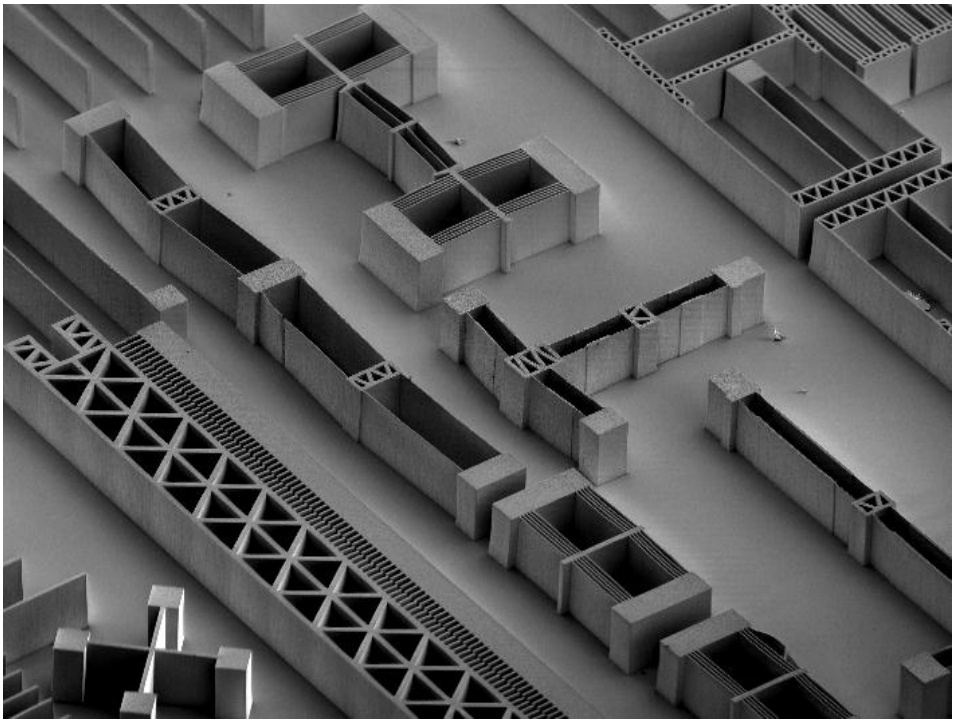

Figure 1.1. These structures are examples of microelectromechanical sytems (MEMS), a kind of microdevice, grown by researchers at Brigham Young University[12].

potential. One primary limitation is the overall robustness and strength of microdevices fabricated from alternative materials. To counter this problem, we follow a recently developed method for the synthesis of nanostructured materials. This method offers the potential to fabricate and characterize high-aspect ratio microstructures made out of various materials, such as amorphous carbon[2].

1.2 Nanostructured Devices

To fabricate microdevices in specific three-dimensional shapes, we add a nanostructured framework that acts as a skeleton template for the deposition of the device material. Due to their vertically-aligned growth and high elasticity, carbon nanotubes (CNTs) have proven to be an excellent material for use as this nanoframework. However, despite their advantageous mechanical properties, weak tensile and

compression strength leaves free-standing CNT templates structurally vulnerable and practically unusable for microdevice fabrication (see Figure 1.2). This problem can be surmounted by infiltrating, or filling, the spaces between the CNTs with another material. Previous experiments have shown amorphous carbon (a-C) to be an attractive choice to act as the infiltrated material due to its relative ease of deposition, handling, and low toxicity. In an effort to understand the thresholds and limits of CNT/a-C structures, we have fabricated and tested sample structures prepared under various conditions to determine the optimum fabrication parameters and the inherent strength of this new composite material. The results of these studies are presented in this thesis.

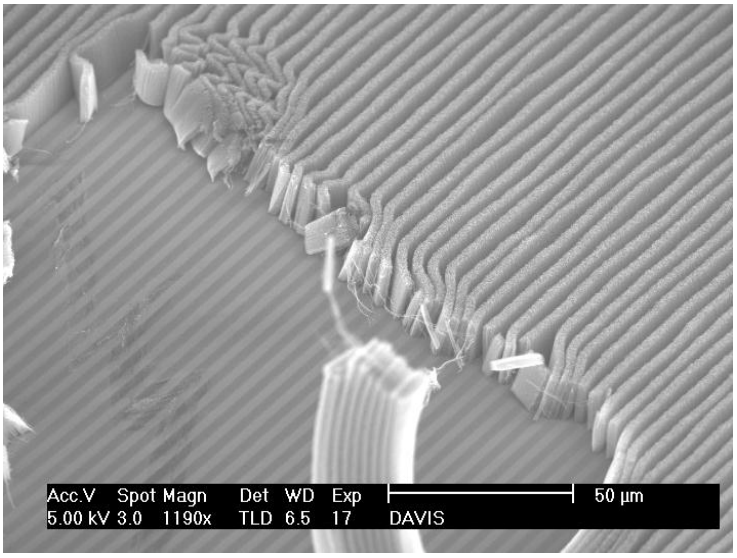

Figure 1.2. Although carbon nanotubes are strong, vertically-aligned forests of carbon nanotubes are weak and impractical for fabrication. This scanning electron microscope image shows damage caused by the light touch of laboratory tweezers. This simple force completely destroyed the carbon nanotube forest.

Chapter 2

Previous Research

2.1 Carbon Nanotubes (CNTs)

2.1.1 History

Carbon nanotubes were identified as a new carbon structure by Sumio Iijima of the NEC laboratories in Japan in 1991. However, carbon fibers were initially used by Thomas Edison as a type of light bulb filament in the late nineteenth century. Shortly thereafter, research on carbon fibers was largely abandoned due to the introduction of tungsten as a superior filament material for incandescent light bulbs. It was not until the late 1950s that carbon was again looked at as a robust and lightweight material for use in the aerospace industry. In the 1970s, significant research was done to optimize the growth process of filamentous carbon fibers through catalytic chemical vapor deposition.

This research laid the groundwork for many processes that were developed to produce carbon fibers for industrial applications in the 1990s[3].

Although these breakthroughs were very influential in the discovery of carbon nanotubes, none was as significant as the discovery of the C_{60}, or buckminsterfullerene, by Kroto and Smalley in 1985 (see Figure 2.1) and the subsequent optimization of its synthesis and growth by Krätscher and Huffman. Sumio Iijima, a Japanese microscopist, took great interest in this work and in 1991 did a detailed transmission electron microscope (TEM) examination of the Krätscher-Huffman carbon samples. He identified the curved, tube-like nanoparticles, now known as multi-walled carbon nanotubes. It was this discovery that propelled carbon nanotubes to the forefront of scientific research[5].

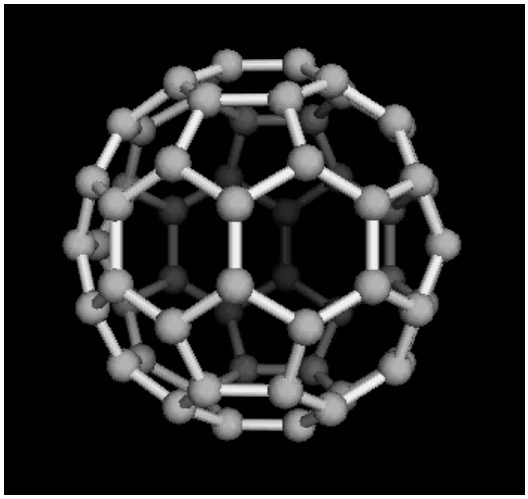

Figure 2.1. This image shows the C_{60} allotrope of carbon, also known as the buckminsterfullerene. The discovery and subsequent research regarding the C_{60} allotrope was instrumental in the identification of carbon nanotubes[4].

Iijima's discovery quickly prompted a theoretical analysis of carbon nanotubes' unique physical properties. These properties were not tested experimentally until 1996, when Smalley of Rice University successfully synthesized aligned single-walled carbon nanotubes[6]. Since then, considerable research has been done to characterize and optimize the properties of carbon nanotubes for eventual use in everyday applications.

2.1.2 Structure

A carbon nanotube is a cylindrical tubule rolled from sheets of carbon graphite called graphene (see Figure 2.2). Bonding in CNTs is almost entirely sp^2 bonding in nature; however, the curvature of CNTs gives rise to the rehybridization of some sp^2 bonds towards sp^3 bonds. This mix of σ and π bonds causes CNTs to be mechanically stronger, electrically and thermally more conductive, and chemically more active than standard graphite materials[7].

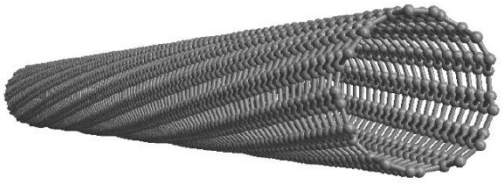

Figure 2.2. Carbon nanotube structure. A carbon nanotube is made from a sheet of graphene that has been rolled to make a tubule. How a nanotube is rolled determines many of its physical properties. Image generated by Brian Davis, Brigham Young University.

CNTs grow in one of two forms: single-walled nanotubes (SWNTs) or multi-walled nanotubes (MWNTs) (see Figure 2.3). A SWNT consists of one nanotube and most have diameters from 1.0-1.4 nm and lengths from 50 to 100 μm. In contrast, a MWNT is comprised of many concentric, coaxial nanotubes. They have outer diameters from 1.4 to 100 nm and can grow to lengths of up to hundreds of micrometers[8].

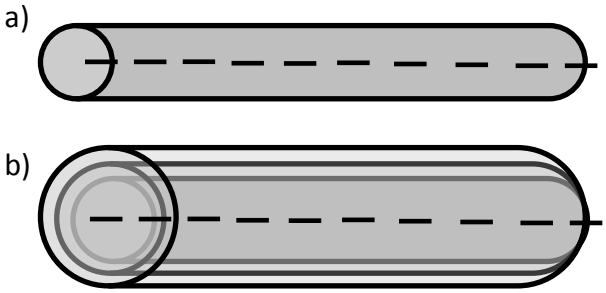

Figure 2.3. Carbon nanotubes grow in one of two forms: a) Single-walled nanotubes (SWNTs) and b) Multi-walled nanotubes (MWNTs). Dashed lines represent the axis of the nanotube. Multi-walled nanotubes are coaxial and concentric.

An ideal, or defect-free, carbon nanotube is comprised of a seamless cylinder of a continuous lattice and can be found in one of three structures. The structure of a

nanotube, or chirality, is described by the chiral vector, **C**, which is expressed as

$$\mathbf{C_h} = n\mathbf{a_1} + m\mathbf{a_2} \qquad (1)$$

where n and m are integers corresponding to the graphite vectors $\mathbf{a_1}$ and $\mathbf{a_2}$ that describe different lattice points (see Figure 2.4). A SWNT is constructed by rolling up a sheet of graphite such that the endpoints of the chiral vector, **C**, are superimposed. This rolling will result in one of three nanotube chiralities: zigzag (n,0), armchair (n,n), or chiral (n,m), where n>m>0[7]. The quantized lattice points (n,m) that define the chirality also define unique geometric and physical properties, such as tube diameter, mechanical strength, and electrical conductivity. Significant research efforts are currently underway to better control the chirality of CNTs so that they can be reliably used in materials applications[8].

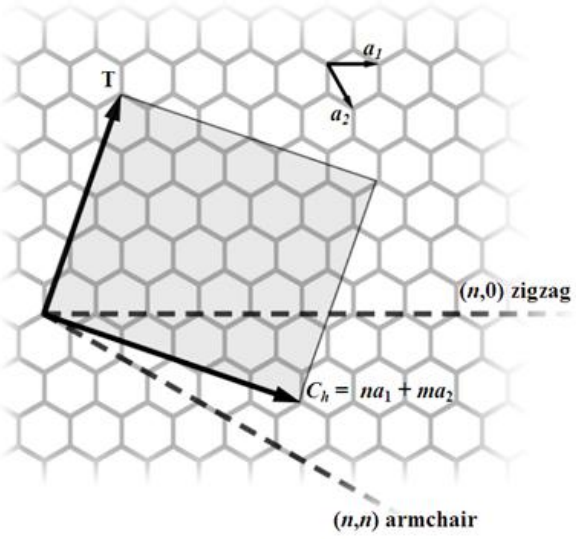

Figure 2.4. The chirality of a carbon nanotube is dependent on the chiral vector $\boldsymbol{C_h}$, which consists of the linear combination of graphitic vectors $\boldsymbol{a_1}$ and $\boldsymbol{a_2}$, that describe the graphene lattice points. These graphitic vectors determine whether a nanotube's chirality is defined as 1) zigzag, 2)armchair, or 3) chiral. The vector, ***T***, represents the axis of the nanotube[9].

Most SWNTs are defect-free. In contrast, most MWNTs contain defects, such as topological flaws, caps, bending, and branching. These defects give rise to slightly different physical properties than those of defect-free nanotubes and should be taken into consideration when characterizing CNTs' properties[7].

2.1.3 CNT Growth Process – Chemical Vapor Deposition

Although there are several methods for CNT synthesis, the scope of this thesis only addresses that of chemical vapor deposition (CVD). CVD is a thermal process by which a carbonaceous feedstock reacts with a catalyst to deposit a carbon structure—in this case, carbon nanotubes. CVD has many advantages, such as its inexpensive apparatus, the ability to run the process at standard ambient temperature and pressure, and the sheer quantity of resultant CNT growth.

Chemical vapor deposition takes place in a quartz tube maintained by a furnace at a temperature between 500 and 1300˚C. Prior to heating the furnace, samples with a catalyst (often Fe or Ni) deposited on the surface are placed into the reaction area of the quartz tube. As the tube heats up to temperature, an inert gas flows through the tube to purge the reactor of any contaminants. Upon reaching the desired temperature, the inert gas is turned off and the carbonaceous gas is introduced into the tube. The catalyst particles then facilitate the disproportionation of the carbonaceous feedstock and the deposition of C in the form of CNTs on the surface of the deposited catalyst. Following the desired growth time, the carbonaceous gas is turned off and the inert gas is reintroduced to the system during cooling. The CNT samples are removed from the tube and exposed to air when the furnace reaches a temperature of approximately 300˚C[8][9]. Using this technique, we can prepare aligned "forests" of MWNTs grown on a patterned catalyst (see Figure 2.5). CNTs maintain this architecture through self-assembly based on Van der Waals forces between neighboring nanotubes[10].

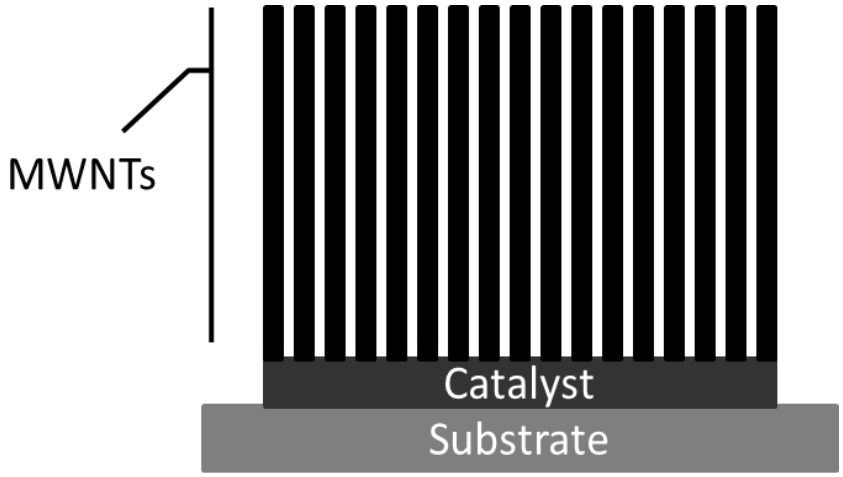

Figure 2.5. Carbon nanotube growth from catalytic chemical vapor deposition. When heated, a disproportionation reaction from a carbonaceous feedstock gas causes carbon nanotubes to grow from a catalyst layer. Nanotube "forests" grow vertically and self-aligning.

2.1.3.1 Effects of Catalyst Thickness

Experimental tests conducted by David Hutchison of Brigham Young University show that the thickness of the Fe catalyst directly affects the quality of the CNT growth[11]. By examining the uniformity and height of nanotube forests grown by varying the Fe-catalyst thicknesses deposited on a 22 nm layer of alumina, Hutchison discovered four factors that affect CNT growth. First, there is a minimum limit for which Fe will catalyze CNT growth. Hutchison suggests that this may be due to the diffusion of small thicknesses of Fe into the alumina layer upon heating the furnace. Second, Fe thicknesses greater than or equal to approximately 20 nm do not catalyze CNT growth. Hutchison suggests that this may be due to the Fe layer remaining a film during the furnace heat-up, thus preventing Fe particles from catalyzing the growth of CNTs. Third, an Fe thickness range of approximately 3-5 nm produces the most uniform and consistent CNTs. Fourth, Fe thicknesses greater than the optimal range result in larger diameter

nanotubes. Based on these data, the thickness of the Fe catalyst was chosen as a variable in our experiment. A value of 4 nm was chosen because it lies in the optimal range for CNT growth and a value of 7 nm Fe was chosen because we theorized that larger tubes might provide an opportunity for more a-C to infiltrate the CNT framework (see Section 3.2).

2.1.4 Mechanical Properties of Carbon Nanotubes

Carbon nanotubes have been a source of great interest in potential structural applications since their discovery due to a favorable aspect ratio, that is to say length-to-diameter ratio[12]. However, materials on the nanoscale do not respond to stimuli in the same way that materials on the macroscale do. Yakobson and Avouris of Rice University and IBM, respectively, state that although it may be appealing to apply standard materials properties definitions to a nanoscale, certain assumptions, such as structural perfection or lack of defects, are often made when making mechanical experimental measurements. Nevertheless, despite their size and the difficulty of mechanical characterization, reliable experimental and theoretical data concerning both SWNTs and MWNTs have been collected and reproduced, most notably for the Young's modulus and tensile (axial) strength.

2.1.4.1 Young's Modulus

The Young's modulus is an important mechanical property that describes the elastic behavior, or stiffness, of a material; it represents the property of a material that corresponds to the mathematical spring constant, *k*, of Hooke's law[13]. Although considerable experimental research using varied methods, such as external load

deflection and resonant electrostatic deflection, has been done to determine the Young's modulus of both SWNTs and MWNTs, the experimental data are inconsistent. However, despite a broad range of values for the Young's modulus of both SWNTs and MWNTs, these data conclusively show that the Young's modulus of SWNTs is consistently higher than that of MWNTs, which varies considerably depending on growth procedure[14]. The average experimental value of SWNTs has been found to be between 1.3-1.8 TPa[12], whereas that of catalytically grown MWNTs has been found to be between 800-900 GPa, depending on growth conditions[15]. This high Young's modulus value characterizes CNTs as one of the most flexible materials on earth (see Table 5.2) and makes them an attractive choice for structural reinforcement applications.

2.1.4.2 Tensile (Axial) Strength

The tensile strength of a material is defined as the maximum stress that a material can withstand in the axial direction. Tensile tests have proven CNTs to be some of the strongest materials in nature. In a recent study by Ming-Fe Yu *et al.*, MWNTs were strength tested in the tensile direction using AFM (atomic force microscope tips) and subsequently analyzed by TEM (transmission electron microscopy). CNTs were found to have a measured tensile strength of approximately 11-63 GPa[16]. When compared to other materials (see Table 5.2), CNTs are considerably stronger.

2.1.4.3 Radial Limitations

The compression, or radial, strength of a material corresponds to the maximum stress a material can withstand in the direction opposite the tensile axis. Although the

tensile strength of CNTs makes them one of the strongest materials found in nature, their compression strength is quite weak in comparison to common materials. Studies have shown that even slight external influences, such as the Van der Waals forces between individual nanotubes, can cause radial deformations[17]. When considered from the radial direction, the Young's modulus of MWNTs drops significantly to a value of approximately 30±10 GPa[18]. Due to this weak compression strength and radial elasticity, CNTs' use in structural applications has been limited. By using CNTs as a structural reinforcement for other materials, these structurally weak properties can theoretically be considerably diminished.

2.2 Amorphous Carbon

2.2.1 Structure and Deposition Procedure

Amorphous carbon (a-C) describes a highly disordered matrix of carbon atoms that are connected with primarily sp^2 bonds (see Figure 2.6). It is an allotrope of carbon that has no crystal structure. Although a-C's structure has next to no long-range ordering, some short-range ordering does exist, which changes considerably depending on the preparation procedure. These changes in short-range ordering and structure significantly affect the properties of the a-C matrix[20].

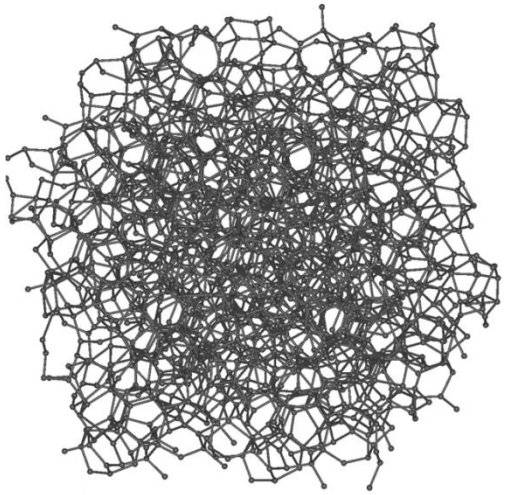

Figure 2.6. Amorphous carbon (a-C). a-C has no crystal structure, but is rather a carbon structure consisting of mostly sp^2 and some sp^3 bonds[19].

Amorphous carbon deposition is a very similar process to chemical vapor deposition; however, no catalyst is required. The same type of furnace that is used for CNT growth is also used for a-C deposition, but the process is carried out at a higher temperature. At these high temperatures and upon passing through an oxygen-free environment, a carbonaceous feedstock gas, such as ethylene, enters into a disproportionation reaction and deposits a-C everywhere in the quartz tube. We have determined that a-C deposition begins at a temperature of approximately 800°C. Because deposition time was presumed to greatly affect the amount of infiltrated a-C, the deposition time was also chosen as a variable to optimize (see Section 4.2).

2.2.2 Mechanical Properties of Amorphous Carbon

The mechanical properties of a-C vary considerably depending on the deposition technique and conditions. Gupta *et al*. found that 400 nm thick a-C deposited by chemical vapor deposition sustained a critical load of 12 mN and had a Young's modulus of 140 GPa—nearly half that of cathodic arc deposition. This is likely due to the dependence of the proportion of sp^2 to sp^3 bonds on the a-C deposition method[21].

2.3 Silicon-Infiltrated Carbon Nanotubes

Prior to the development of this project, Hutchison *et al*. of Brigham Young University characterized a CNT/Si nanocomposite material for use in microfabrication. Nanostructured CNTs were grown through CVD and subsequently infiltrated with polycrystalline silicon using low pressure chemical vapor deposition (LPCVD). This nanocomposite material was found to have a Young's modulus of 120 GPa—a value

slightly lower than that of polycrystalline silicon (140-210 GPa) [22]. This lower value is attributed to large voids that form during LPCVD as some areas are shut off from further deposition. SEM imagery revealed that the volume of CNTs compared to the silicon filler was so small that their contribution to the Young's modulus was insignificant.

Chapter 3

Experimental Methods

3.1 Fabrication Process Overview

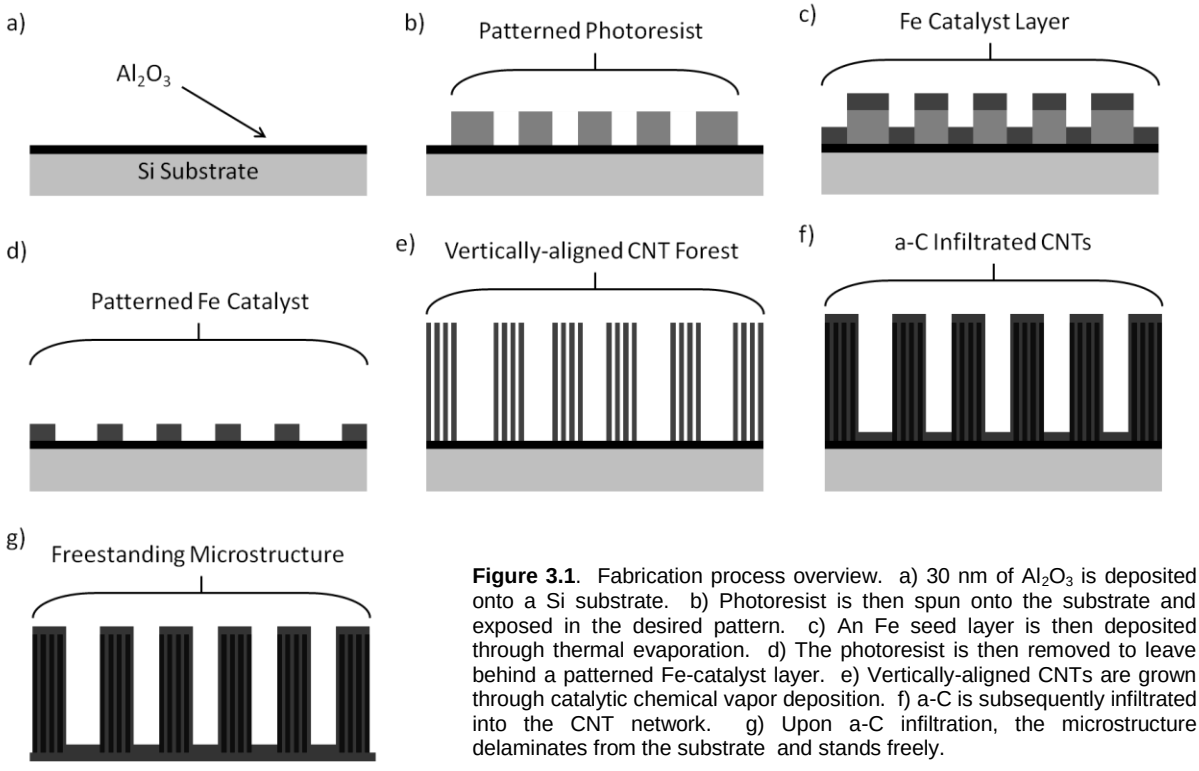

Figure 3.1. Fabrication process overview. a) 30 nm of Al_2O_3 is deposited onto a Si substrate. b) Photoresist is then spun onto the substrate and exposed in the desired pattern. c) An Fe seed layer is then deposited through thermal evaporation. d) The photoresist is then removed to leave behind a patterned Fe-catalyst layer. e) Vertically-aligned CNTs are grown through catalytic chemical vapor deposition. f) a-C is subsequently infiltrated into the CNT network. g) Upon a-C infiltration, the microstructure delaminates from the substrate and stands freely.

3.2 Mask Design

A mask intended for use in photolithography was designed specifically for our experiment. Using Adobe Photoshop®, we made a mask with 13 cantilevers of length 2.2 mm and width 300 μm extending from a single base (see Figure 3.2a). Triangular markers were integrated into the mask on each of the cantilevers' three sides to indicate the exact location of the center 2 mm point for ease in experimental testing (see Figure 3.2b).

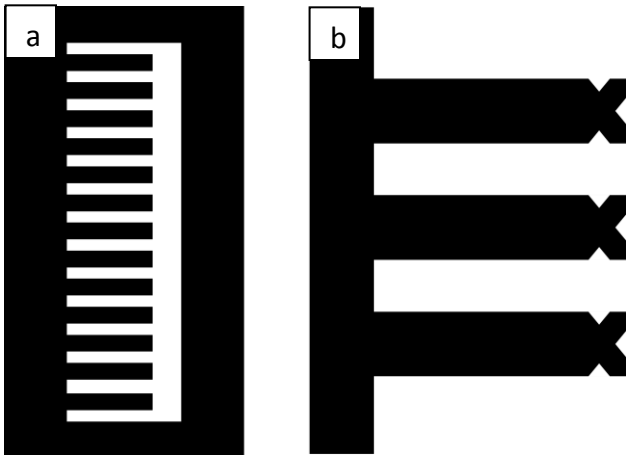

Figure 3.2. a) Mask design containing 13 cantilever beams connected to a support structure. b) Detail of cantilever beams. Triangular markers indicate the center 2 mm mark, where experimental testing will occur.

3.3 Design of Experiment

We employed design of experiment (DOE) principles in our experimentation, which allowed us to test multiple independent variables simultaneously while focusing on one specific area of interest. A full factorial experiment with two independent variables (A, B) and two levels per variable (a1, a2, b1, b2) was used. We held one variable constant while varying the other to give a total of four test parameters: (a1,b1), (a1,b2), (a2,b1), and (a2,b2) (see Figure 3.3). These four parameters acted as upper and lower bounds on our experiment and allowed us to examine their effects on our results within that specific area of interest. We chose the thickness of the Fe catalyst and the a-C

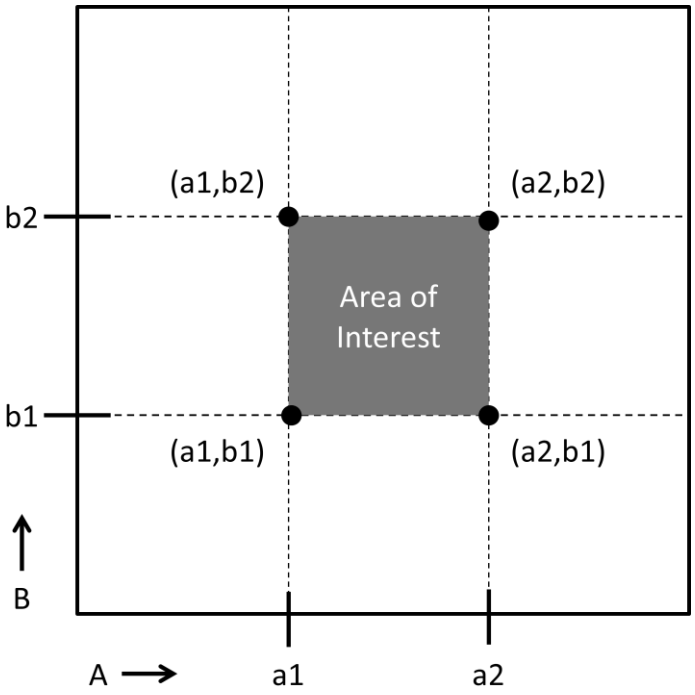

Figure 3.3. Graphical representation of a full factorial design of experiment. Each axis represents an independent variable with two different levels. One variable is held constant while the other is changed. An investigation of every possibility yields four experimental parameters. These four test parameters set bounds for a specific area of interest.

deposition time as our independent variables. Values of 4 nm and 7 nm of Fe were chosen as low and high levels for the Fe thickness, while values of 30 minutes and 120 minutes were chosen as low and high levels for the a-C infiltration time.

3.4 Wafer Preparation

Wafer preparation began by depositing 30 nm of alumina (Al_2O_3) onto a four-inch Si wafer through electron beam (E-Beam) evaporation at a pressure below 10 μTorr. The wafer was then cleaned by rinsing vigorously with acetone followed by isopropyl alcohol. It was subsequently blown dry with nitrogen gas to prevent solvent residue from drying on the sample. Following solvent cleaning, the wafer underwent a dehydration

bake for 8 minutes at a temperature of 150° C to remove any internally absorbed moisture.

AZ3312 photoresist was then spin-coated at 4000 rpm for 1 minute onto the wafer to a thickness of approximately 1 μm and soft-baked on a hot plate at a temperature of 90° C for 1 minute. The photoresist was subsequently exposed by 385 nm ultraviolent light in a cantilever pattern specifically designed for this experiment (Karl Suss Mask Aligner, MA 150 CC used for photolithographic procedure). The wafer was then submerged in an AZ300MIF developer solution for approximately 35 seconds, thus removing the exposed photoresist, after which it was rinsed with distilled water and blown dry with air. Finally, the wafer was hard-baked on a hot plate at a temperature of 90° C for 1 minute to allow handling of the wafer without danger of further photoresist exposure.

Fe was then deposited on the wafer as a catalytic seed layer. Roughly half of the samples were coated with 4 nm of Fe and the other half were coated with 7 nm of Fe. The deposition of both thicknesses occurred through thermal evaporation at a pressure below 5 μTorr at a rate of 0.1 nm /second.

After Fe deposition, the wafer was submerged into Shipley Microposit 1165 resist stripper to remove the excess photoresist, leaving an Fe seed layer in the desired exposed pattern. To prevent residue from the Microposit 1165 from drying onto our sample, the wafer was again rinsed clean with acetone and isopropyl alcohol and subsequently dried with flowing nitrogen gas.

3.5 Carbon Nanotube (CNT) Growth

Patterned wafers were then cut into individual samples with a diamond scribe and placed in a one-inch diameter tube furnace for carbon nanotube growth and carbon deposition. Carbon nanotubes were grown by chemical vapor deposition (see section 2.3.1) on the patterned Fe at a temperature of 750° C for 6 minutes using a mixture of 193 sccm hydrogen (H_2) gas and 129 sccm ethylene (C_2H_4) as the feedstock gas. This growth formed a cantilever structure, which was then used as a nanoframework for a cantilever microdevice.

3.6 Carbon Infiltration

Following CNT growth, the wafers were placed in a furnace and heated to 900° C. A mixture of 199.5 sccm argon (Ar) and 189.9 sccm C_2H_4 gases were flowed through the furnace, depositing amorphous carbon through chemical vapor deposition (see section 3.1). Half of the 7 nm Fe samples were infiltrated with carbon for 30 minutes, while the remaining half was infiltrated for 120 minutes. Similarly, approximately half of the 7 nm Fe samples were infiltrated with C for 30 minutes, while the remaining half was infiltrated for 120 minutes. During the deposition process, the CNT-templated samples delaminated from the silicon substrate and, following cooling, were removed from the furnace in preparation for experimental testing.

3.6.1 Removal of Floor Layer

Because layers of a-C deposit everywhere on the sample, both in areas with and without nanotubes, some samples delaminated from the Si substrate with an a-C "floor

layer" remaining connected to the microstructure. These floor-layer samples were cleaned using a planar plasma etcher at 100 W in one-minute increments until clean. We assume that this process had no effect on the resultant properties of the microstructure.

3.7 Experimental Testing

Each of the 13 cantilevers contained in each sample was tested using an Instron materials testing apparatus. A needle connected to a force transducer slowly depressed each cantilever at a rate of 0.5 mm/minute at a distance of 2 mm from its base until catastrophic failure (see Figure 3.4). The resultant force resistance in Newtons per millimeter was then recorded by the Instron apparatus and kept for further analysis.

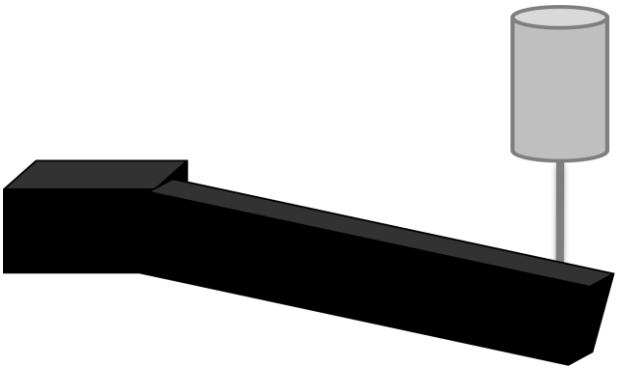

Figure 3.4. Samples were tested using a needle connected to a force transducer. Each cantilever beam was depressed until catastrophic failure while measurements of extension vs. applied force were recorded.

3.7.1 Apparatus Design

In order to secure samples for testing, a sample holder was designed specifically for this experiment (see Figure 3.5). Because each sample was depressed downward from above, a small well was milled in the center of an aluminum block that allowed each cantilever to deflect downwards. Clamps were added to the aluminum block to securely hold each sample in place. The sample holder was then placed onto an x-y micrometer translation stage to facilitate the alignment of consecutive cantilever tests.

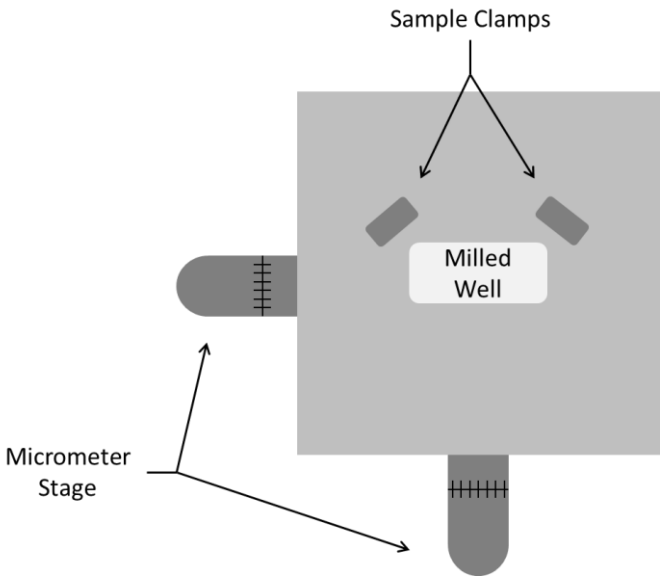

Figure 5.5. Top view of sample holder. Samples were clamped over the milled well to allow cantilever beam depression and attached to a micrometer stage to facilitate cantilever beam alignment.

Chapter 4

Data and Results

4.1 Visual Examination of Samples

An examination by optical microscopy shows that the CNT matrix grew vertically aligned, following our designed photolithography mask (See Figure 4.1).

Figure 4.1. Two cantilever beams shown through optical microscopy. Each sample had thirteen such beams. The support frame is seen on the left and represents the fixed end of each cantilever. The triangular markings on the right-hand side facilitate experimental testing.

As seen in Figure 4.1, microcantilever beams extend from a support frame on the left. Triangular markers indicate the approximate location of the applied force during testing. The excess material on the outside of the cantilever beams show remnants of the floor layer (See section 3.6.1) and is a vestige of the a-C infiltration process; however, this

material does not affect the force measurements in any way. These observations are typical of all samples, although some contain slight surface deformations on the base sections of the samples. These are likely due to impurities on the sample pattern prior to CNT growth; however, we do not expect these deformations to adversely affect experimental measurements as they are not found on the actual cantilever beams.

4.2 Numerical Materials Properties Extraction

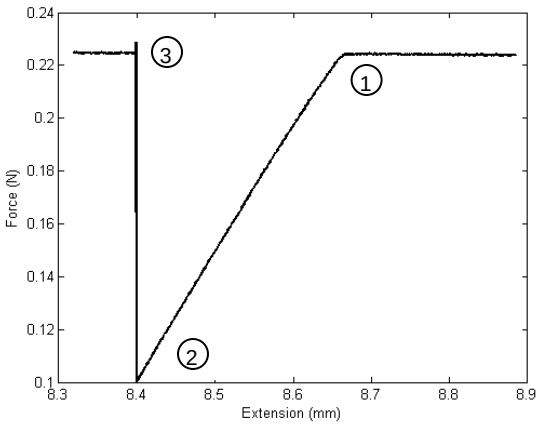

Figure 4.2. Extension vs. applied force graph as obtained experimentally. Position 1 indicates the point at which the needle began to apply a load to the cantilever beam. Position 2 shows the point at which the cantilever broke. The steep slope between position 2 and position 3 indicates that little or no plastic deformation occurred during this test. These data are typical of all cantilever tests.

Raw numerical data of applied force vs. position (see Figure 4.2) as measured by the Instron 3342 materials testing apparatus was analyzed and examined to extract both the Young's modulus and the yield stress. Following the basic cantilever beam equation with boundary conditions for a beam fixed at one end, the Young's modulus and yield stress were found through the following equations:

$$E = \frac{4Fl^3}{dwt^3} \qquad (2)$$

$$\sigma = \frac{6lF_{max}}{wh^2} \qquad (3)$$

where E is the Young's modulus, σ is the yield stress, *d* is the vertical distance of the beam's deflection, *w* is the width of the beam, *l* is the distance from the fixed end to the applied force, *t* is the thickness of the beam, *F* is the applied force, and F_{max} is the

maximum applied force at the beam's breaking point. Data from experimental testing provided us with the values of the beam deflection and the maximum applied force. Beam width and length were defined by the mask design. CNT growth time was chosen to produce structure thicknesses of 200 μm. However, due to slight variation in growth conditions, exact beam thicknesses were measured using scanning electron microscopy (SEM). Each sample was designed to yield 13 cantilever beams for reproducibility. Displacement vs. load was measured for each of the cantilevers and the Young's modulus and yield stress were calculated. The values of each beam were then averaged to give average Young's modulus and average yield stress per sample. Samples were then compared to reveal which set of parameters affected the mechanical properties of our material most. Some of the following data are not based on 13 beam samples, as not all beams survived the delamination from the substrate. (See Appendix I for full experimental data).

4.3 Young's Modulus and Yield Stress of CNT/a-C Nanocomposite

Table 4.1 shows the average measured Young's modulus for samples grown at different parameters. We expected to see a reflection of the extraordinarily high Young's modulus value of CNTs in the carbon nanocomposite material; however, the low values of our CNT/a-C nanocomposite indicate that the CNTs probably contribute minimally to the Young's modulus. This could be due to poor load transfer between the a-C and the CNT nanoframework. When compared to that of other materials, our measured data show the Young's modulus of the CNT/a-C nanocomposite to be significantly lower (see

Table 4.1). This characterizes our nanocomposite as a relatively flexible material with respect to standard construction materials.

Table 4.1 also shows the average measured yield stress for samples grown at different parameters. These data show that the yield stress of the CNT/a-C nanocomposite is similar to that of other materials (see table 4.2). This indicates that our material can withstand loads comparable to that of polycarbonate before catastrophic failure.

	4 nm Fe / 30 Minute Infiltration	4 nm Fe / 120 Minute Infiltration	7 nm Fe / 30 Minute Infiltration	7 nm Fe / 120 Minute Infiltration
Young's Modulus (GPa)	1.67	2.02	7.87	4.98
Yield Stress (MPa)	53.7	60.3	147	87.1

Table 4.1. Average Young's modulus and average stress values for each experimental parameter. The sample grown from 7 nm thick Fe catalyst and infiltrated for 30 minutes shows the maximum mechanical properties.

	CNT / a-C Nanocomposite	Single-walled Carbon Nanotube	Cast Iron	Carbon Steel	Aluminum Alloys	Polycarbonate
Young's Modulus (GPa)	1.67 – 7.87	1300 – 1800*	103.4	206.8	71.7	2.4
Yield Stress (MPa)	53.7 – 147	---	290	300 – 1000*	100 – 300*	62.1

Table 4.2. Average Young's modulus and average stress values for common materials. Comparisons of these values characterize our material as a moderately strong, flexible material.[8] *Different treatments of same material results in different Young's modulus and yield stress values, as reflected by the data ranges[14].

4.4 Effects of a-C Infiltration Time on Mechanical Properties

Figures 4.3a and 4.3b respectively show the effects of the a-C infiltration time on the average Young's modulus and yield stress per sample. Dark bars represent samples that have been infiltrated for 30 minutes and light grey bars represent samples that have been infiltrated for 120 minutes. We expected to see a distinct difference between samples that were infiltrated for longer amounts of time due to the deposition of more

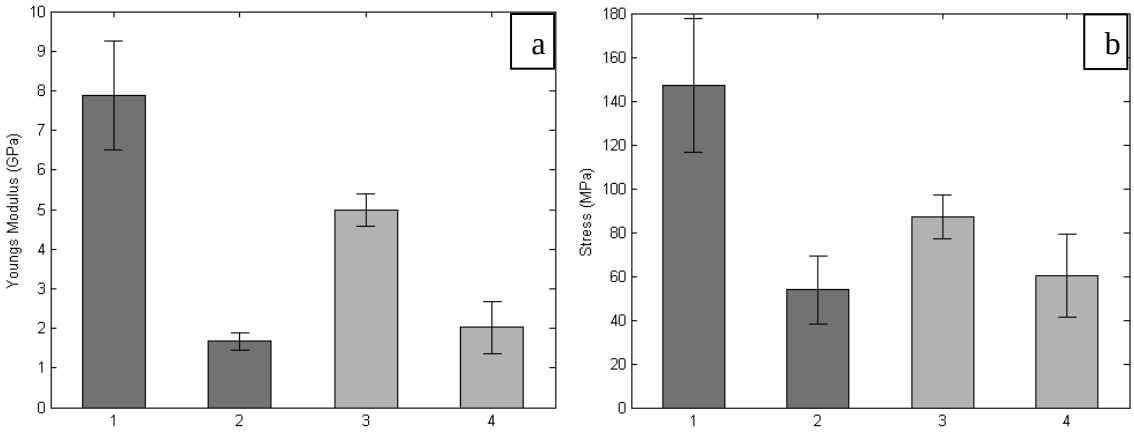

Figure 4.3. a) Average Young's modulus values classified by a-C infiltration time. Dark grey bars represent structures that were infiltrated for 30 minutes, while light grey bars represent structures that were infiltrated for 120 minutes. Data within each infiltration time vary considerably, indicating little or no dependence on a-C infiltration time beyond that of normal fabrication variation. b) Average yield stress values classified by a-C infiltration time. Again, dark grey bars represent structures that were infiltrated for 30 minutes, while light grey bars represent structures that were infiltrated for 120 minutes. Yield stress data within each infiltration time also vary somewhat, indicating that the a-C infiltration time did not significantly affect the yield stress of the structure. Error bars show the standard deviations for each sample.

carbonaceous material. Surprisingly, we found that the Young's modulus of the samples that were infiltrated for 30 minutes did not vary considerably from samples that were infiltrated for 120 minutes at the same Fe-catalyst thickness. Each infiltration time resulted in some samples with low and some with high Young's modulus values, indicating no infiltration time dependence, but some uncontrolled synthesis parameters. Results for the yield stress also followed this pattern, though to a lesser degree.

Because additional a-C material should fill more voids and thus result in some change in materials properties, we determined that the amount of infiltrated a-C must be approximately equal for samples of both infiltration times. SEM imagery revealed that at some point during infiltration, a "cap" of a-C (see Figure 4.4) formed around our structures, effectively sealing the CNT matrix from additional a-C deposition. To study this phenomenon, a test sample grown from a 7 nm thick Fe catalyst was infiltrated for 120 minutes, but at a lower temperature of 800˚ C to retard the deposition rate. a-C carbon infiltration was significantly decreased as evidenced by the lack of delamination

from the Si substrate after infiltration. SEM imagery shows that unlike the samples infiltrated at 900˚ C, this sample did not form a cap around the outside of the sample (see Figure 4.5). However, Figure 4.5 also shows a considerable decrease in infiltrated material. It is possible that a longer infiltration time at a lower temperature would still result in enough infiltrated material to cause a structural cap. Further research must be done to explore the full effects of a-C infiltration temperature.

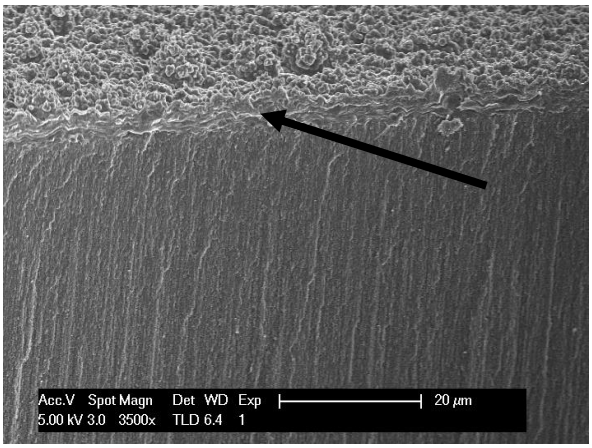

Figure 4.4. Scanning electron microscope image of a-C infiltrated carbon nanotubes. The arrow points to a "cap" that effectively covered and sealed the structure, thus preventing additional a-C deposition.

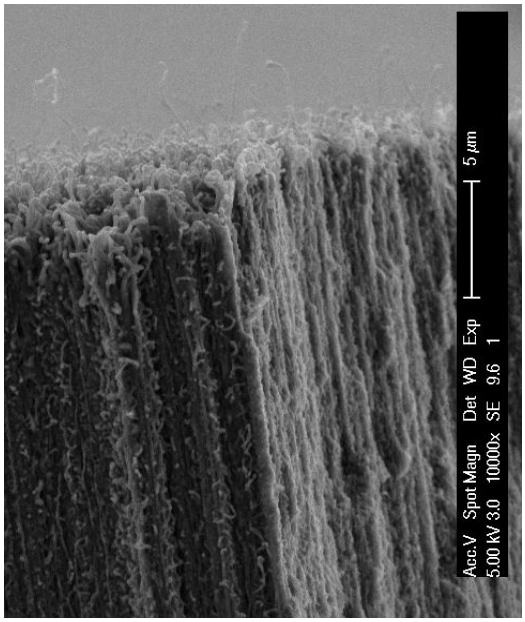

Figure 4.5. Scanning electron microscope image of carbon nanotubes infiltrated with a-C at 800° C for 120 minutes. The "capping" effect noticed at depositions of higher temperatures is missing in this sample; however, it also exhibits a decreased amount of infiltrated material.

4.5 Effects of Fe Thickness on Mechanical Properties

Figures 4.6a and 4.6b respectively show the effects of the Fe thickness on the Young's modulus and yield stress per beam per sample. Dark grey bars represent samples upon which a 7 nm Fe catalyst was deposited, while light grey bars represent samples upon which a 4 nm Fe catalyst was deposited. These data show that the thicker 7 nm Fe catalyst consistently resulted in a higher Young's modulus than that of the 4 nm Fe catalyst. The yield stress was also clearly higher for 7 nm thick seed layers, though to a lesser extent. This suggests that a wider CNT diameter (see Section 2.1.3.1) results in higher mechanical properties, especially Young's modulus.

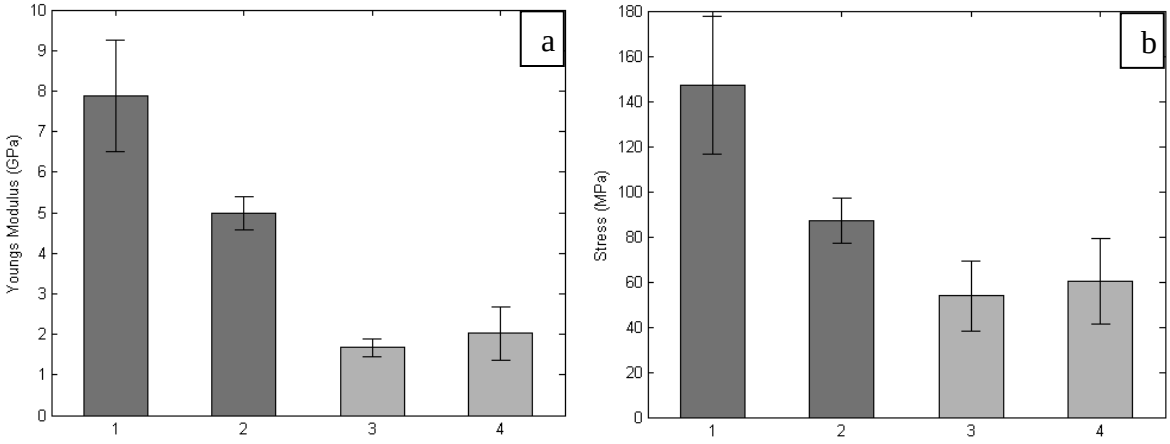

Figure 4.6. a) Average Young's modulus values classified by Fe catalyst thickness. Dark grey bars represent samples whose CNTs were grown from 7nm Fe-catalyst thicknesses. Light grey bars represent samples whose CNTs were grown from 4 nm Fe-catalyst thicknesses. These data clearly show that a thicker Fe catalyst results in a higher Young's modulus. b) Average yield stress values classified by Fe-catalyst thickness. Dark grey bars represent samples whose CNTs were grown from 7nm Fe-catalyst thicknesses. Light grey bars represent samples whose CNTs were grown from 4 nm Fe-catalyst thickness. Like the Young's modulus data, a thicker Fe-catalyst layer also results in a higher yield stress, though to a lesser degree. Error bars show the standard deviations for each sample.

4.6 Scanning Electron Microscopy Examination (SEM) of Samples

After experimental testing, scanning electron microscopy (SEM) was used to visually analyze the structure and qualitatively examine the amount of void space of each

sample. Each sample was imaged at the point of cantilever failure to expose a cross-sectional area of the nanocomposite structure. Regardless of test parameter, we found every sample to have considerable void space (see Figures 4.7a-d). However, a visual comparison of samples grown from 4 nm Fe catalysts and samples grown from 7 nm Fe catalysts suggest that a 7 nm thick Fe seed layer resulted in a slightly less-filled interior than those grown from a 4 nm thick seed layer. These results proved to be contrary to our expectations. These images show that samples with *more* void space—and thus less infiltrated material—consistently resulted in higher mechanical properties.

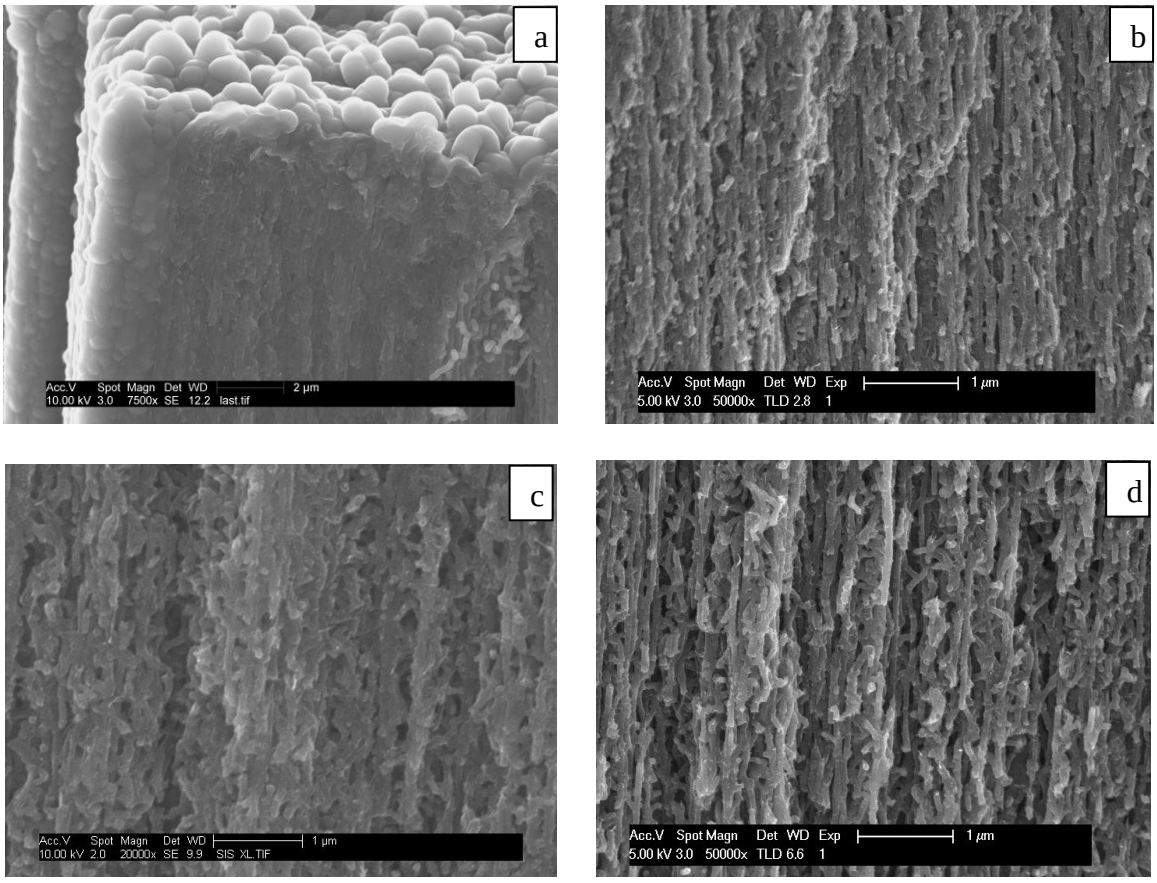

Figure 4.7. Cross-sectional SEM images of samples grown at different conditions. a) Sample grown from 4 nm thick Fe-catalyst layer and a-C infiltrated for 30 minutes. b) Sample grown from 4 nm thick Fe-catalyst layer and a-C infiltrated for 120 minutes. c) Sample grown from 7 nm thick Fe-catalyst layer and a-C infiltrated for 30 minutes. d) Sample grown from 7 nm thick Fe-catalyst layer and a-C infiltrated for 120 minutes. All samples show low amount of infiltrated material and high amount of void space; however, a comparison between samples grown from 4 nm thick Fe-catalyst layers and 7 nm thick Fe-catalyst layers reveal that the latter contain more void space.

4.7 Effects of Annealing on Mechanical Properties

After examining samples corresponding to our 4 experimental parameters, the effects of sample annealing was partially explored. One sample of each Fe thickness was fabricated and subsequently annealed in a one-inch tube furnace at 900˚ C in flowing hydrogen gas. Samples were tested in the same manner as the unannealed samples. When compared to their unannealed counterparts, the annealed samples corresponding to both Fe thicknesses showed a noticeable increase in Young's modulus and yield stress (see Figures 4.8a-b). This is likely due to slight structural changes or the introduction of defects in the CNT/a-C nanocomposite when exposed to high temperatures. These structural changes appear to improve the strength of this material, though further testing will be required to understand the extent to which this trend occurs.

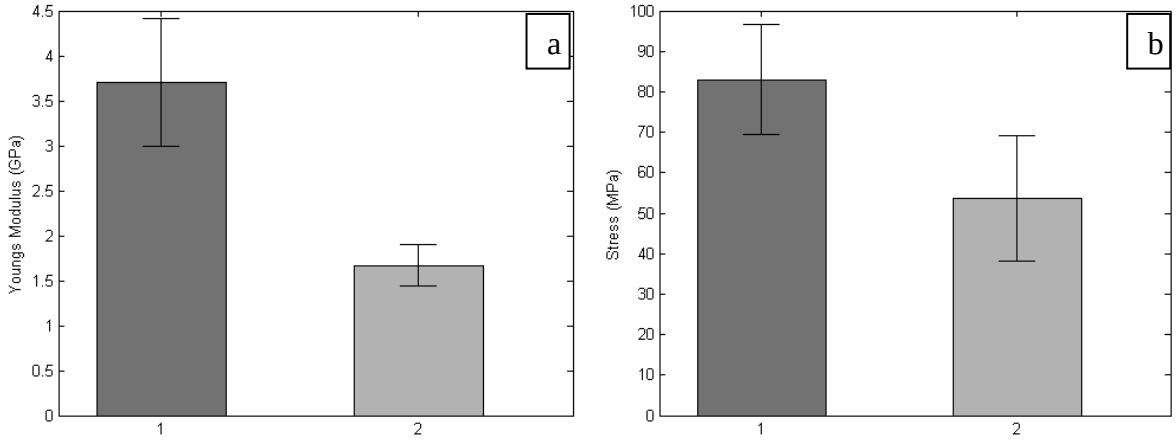

Figure 4.8. Young's modulus (a) and yield stress (b) for unannealed and annealed samples. Dark grey bars represent a sample grown from 4 nm thick Fe-catalyst layers, infiltrated for 30 minutes, and subsequently annealed at 900˚ C in flowing hydrogen gas. Light grey bars represent an unannealed sample grown at identical conditions. These data show that the annealed sample has a higher Young's modulus and a higher yield stress than the unannealed sample. Additional research is needed to further characterize this effect. Error bars show the standard deviations for each sample.

Chapter 5

Conclusions and Future Directions

In this study we have characterized the Young's modulus and the yield stress of a new carbon nanotube/amorphous carbon nanocomposite material. We applied a full factorial experimental design to test the effects of the Fe seed layer thickness and the a-C infiltration time on the mechanical properties of the material. Following this model, carbon nanotubes were grown as a nanoframework by chemical vapor deposition on an Fe seed layer and subsequently infiltrated with a-C for different lengths of time to produce microcantilever structures. These microcantilever structures were then force tested and the Young's modulus and yield stress were calculated.

We expected to see an increased material strength with a longer a-C infiltration time. However, our results indicated that the infiltration time had a negligible effect on the mechanical properties of the nanocomposite material. We postulate that this is due to an a-C cap that forms around the outside of the structure upon infiltration. The thickness

of the Fe catalyst did have a significant effect on measured mechanical properties. We found that a thicker Fe seed layer results in a higher Young's modulus and yield stress of the material.

The resulting Young's modulus and yield stress data for the material characterize it as quite flexible with a moderate strength, making it advantageous for use in applications requiring a high compliance. Although this material has proven to be interesting and potentially useful in commercial applications, additional research must be done to further optimize CNT growth conditions and a-C infiltration parameters. This study has provided useful information for further study of annealing and alternative infiltration temperatures—two factors we hope will help us more fully characterize the material properties of the nanocomposite.

Microdevices such as humidity sensors and accelerometers are already changing the face of technology. Carbon nanotube-templated materials have the potential to significantly enhance their functionality and overall robustness. We hope that with further research they will soon be introduced into mainstream industrial fabrication processes.

References

[1] Poole, Charles P. and Owens, Frank J. *Introduction to Nanotechnology*. Hoboken, New Jersey: John Wiley & Sons, Inc (2003).

[2] Hutchison, David N., *et al*. "High Aspect Ratio Microelectromechanical Systems: A Versatile Approach Using Carbon Nanotubes as a Framework." Proc. 15th Int. Conf. on Solid-State Sensors, Actuators and Microsystems (2009).

[3] Saito, R., Dresselhaus, G., and Dresselhaus, M. H. *Physical Properties of Carbon Nanotubes*. London, UK: Imperial College Press (1998).

[4] Mehrotra, Saumitra R. and Klimeck, Gerhard. Derivative work by Akkakk. http://commons.wikimedia.org/wiki/File:C60_Buckyball_croped.gif. Licensed under the Creative Commons Attribution 3.0 Unported license.

[5] Harris, Peter J. F. *Carbon Nanotubes and Related Structures: New Materials for the Twenty-first Century*. Cambridge, UK: Cambridge University Press (1999).

[6] Dresselhaus, M.S. and Avouris, Phaedon. "Introduction to Carbon Materials

Research." *Carbon Nanotubes: Synthesis, Structure, Properties, and Applications.* M. S. Dresselhaus, G. Dresselhaus, and Ph. Avouris, Eds. Berlin: Springer (2000).

[7] Han, Jie. "Structure and Properties of Carbon Nanotubes." *Carbon Nanotubes: Science and Applications.* Meyyappan, M., Ed. Boca Raton, FL: CRC Press LLC (2005).

[8] Srivastava, C. M. and Srinivasan, C. *Science of Engineering Materials and Carbon Nanotubes* (3rd Edition). Kent, UK: New Age Science Limited (2010).

[9] Meyyappan, M. "Growth: CVD and PECVD." *Carbon Nanotubes: Science and Applications.* Meyyappan, M., Ed. Boca Raton, FL: CRC Press LLC (2005).

[10] Dai, Hongie. "Nanotube Growth and Characterization." *Carbon Nanotubes: Synthesis, Structure, Properties, and Applications.* M. S. Dresselhaus, G. Dresselhaus, and Ph. Avouris, Eds. Berlin: Springer (2000).

[11] Hutchison, David N. "Vertically Aligned Carbon Nanotubes as a Framework for Microfabrication of High Aspect Ratio MEMS." Undergraduate thesis, published by Brigham Young University Department of Physics and Astronomy (2008).

[12] Yakobson, Boris I. and Avouris, Phaedon. "Mechanical Properties of Carbon Nanotubes." *Carbon Nanotubes: Synthesis, Structure, Properties, and Applications.* M.S. Dresselhaus, G. Dresselhaus, and Ph. Avouris, Eds. Berlin: Springer (2000).

[13] Norton, Robert L. *Machine Design: An Integrated Approach* (3rd Edition). New Jersey: Pearson Prentice Hall (2006).

[14] Forró, László and Shönenberger, Christian. "Physical Properties of Multi-Wall Nanotubes." *Carbon Nanotubes: Synthesis, Structure, Properties, and Applications.* M.S. Dresselhaus, G. Dresselhaus, and Ph. Avouris, Eds. Berlin: Springer (2000).

[15] Demczyk, B.G., *et al.* "Direct mechanical measurement of the tensile strength and elastic modulus of multiwalled carbon nanotubes." *Materials Science and Engineering A.* **334** (2002) 173–178.

[16] Min-Feng Yu, *et al.* "Strength and Breaking Mechanism of Multiwalled Carbon Nanotubes Under Tensile Load." *Science* **287**, 637 (2000).

[17] Ruoff, Rodney S., *et al.* "Radial deformation of carbon nanotubes by van der Waals forces." *Nature* **364**, 6437 (1993).

[18] Palaci, I., *et al.* "Radial Elasticity of Multiwalled Carbon Nanotubes." *Physical Review Letters* **94**, 175502 (2005).

[19] Ströck, Michael. Derivative work by Mahahahaneapneap. http://upload.wikimedia.org/wikipedia/commons/f/f8/Eight_Allotropes_of_Carbon.png. Licensed under the Creative Commons Attribution-Share Alike 3.0 Unported license.

[20] Dresselhaus, M. S., Dresselhaus, G., and Eklund, P. C. *Science of Fullerenes and Carbon Nanotubes*. London, UK: Academic Press, Inc. (1996).

[21] Gupta, B. K. and Bhushan, Bharat. "Mechanical properties of amorphous carbon coatings deposited by different deposition techniques." *Thin Solid Films* **270**

(1995) 391-398.

[22] Hutchison, David N., *et al*. "Carbon nanotubes as a framework for high aspect ratio MEMS fabrication." *J. MEMS* **19**, 1 (2010) 75-82.

APPENDIX I

The following data represent the extension (mm) and load (N) information used to calculate the Young's modulus and yield stress for each sample. Sample 1: 7 nm Fe Catalyst / 30 minute a-C infiltration. Sample 2: 4 nm Fe Catalyst / 30 minute a-C infiltration. Sample 3: 4 nm Fe Catalyst / 120 minute a-C infiltration. Sample 4: 4 nm Fe Catalyst / 30 minute a-C infiltration / 30 minute anneal. Sample 5: 7 nm Fe Catalyst / 120 minute a-C infiltration.

Sample 1	Load (N)	E (Pa)	Stress (Pa)	% Strain		
1	1.24E-01	9.20E+09	1.60E+08	1.74E+00		
2	1.27E-01	9.02E+09	1.63E+08	1.81E+00		**Average**
3	1.33E-01	7.91E+09	1.72E+08	2.18E+00	**Load (N)**	1.14E-01
4	9.65E-02	7.29E+09	1.25E+08	1.71E+00	**E (Pa)**	7.87E+09
5	1.06E-01	6.76E+09	1.37E+08	2.03E+00	**Stress (Pa)**	1.47E+08
6	1.31E-01	7.07E+09	1.69E+08	2.40E+00	**Strain**	1.89E+00
7	1.10E-01	6.86E+09	1.42E+08	2.07E+00		
8	7.85E-02	6.73E+09	1.01E+08	1.51E+00		**Max**
9	1.30E-01	6.79E+09	1.68E+08	2.48E+00	**Load (N)**	1.33E-01
10	1.29E-01	7.59E+09	1.66E+08	2.19E+00	**E (Pa)**	1.10E+10
11	5.78E-02	6.69E+09	7.47E+07	1.12E+00	**Stress (Pa)**	1.60E+08
12	1.29E-01	9.40E+09	1.66E+08	1.77E+00	**Strain**	2.48
13	1.29E-01	1.10E+10	1.66E+08	1.51E+00		
AVG		7.87E+09	1.47E+08			**Min**
ST DEV		1.37E+09	3.04E+07		**Load (N)**	5.78E-02
					E (Pa)	6.69E+09
					Stress (Pa)	7.47E+07
					Strain	1.12

Sample 2	Load (N)	E (Pa)	Stress (Pa)	% Strain		
1	1.31E-01	1.88E+09	6.83E+07	3.63E+00		
2						**Average**
3	3.28E-02	1.70E+09	1.71E+07	1.00E+00	**Load (N)**	1.03E-01
4	1.35E-01	1.67E+09	7.06E+07	4.23E+00	**E (Pa)**	1.67E+09
5	1.12E-01	1.47E+09	5.84E+07	3.97E+00	**Stress (Pa)**	5.37E+07
6	1.27E-01	1.43E+09	6.60E+07	4.62E+00	**Strain**	3.30E+00
7	1.05E-01	1.39E+09	5.48E+07	3.94E+00		
8	1.07E-01	1.53E+09	5.57E+07	3.64E+00		**Max**
9					**Load (N)**	1.31E-01
10					**E (Pa)**	2.10E+09
11	1.01E-01	1.64E+09	5.28E+07	3.22E+00	**Stress (Pa)**	7.06E+07
12	9.58E-02	1.87E+09	5.00E+07	2.67E+00	**Strain**	4.62
13	8.36E-02	2.10E+09	4.36E+07	2.08E+00		
AVG		1.67E+09	5.37E+07			**Min**
ST DEV		2.28E+08	1.54E+07		**Load (N)**	3.28E-02
					E (Pa)	1.39E+09
					Stress (Pa)	1.71E+07
					Strain	1

Sample 3	Load (N)	E (Pa)	Stress (Pa)	% Strain		
1	1.33E-01	3.08E+09	9.10E+07	2.95E+00		
2	7.73E-02	1.84E+09	5.28E+07	2.87E+00		**Average**
3	7.10E-02	2.00E+09	4.85E+07	2.43E+00	**Load (N)**	8.82E-02
4	1.06E-01	2.10E+09	7.25E+07	3.45E+00	**E (Pa)**	2.02E+09
5					**Stress (Pa)**	6.03E+07
6					**Strain**	3.03E+00
7	8.96E-02	1.94E+09	6.12E+07	3.15E+00		
8						**Max**
9	1.02E-01	1.99E+09	6.94E+07	3.49E+00	**Load (N)**	1.33E-01
10	2.55E-02	5.17E+08	1.74E+07	3.37E+00	**E (Pa)**	3.08E+09
11	9.50E-02	2.07E+09	6.49E+07	3.14E+00	**Stress (Pa)**	9.10E+07
12	8.40E-02	1.98E+09	5.74E+07	2.90E+00	**Strain**	3.49
13	9.87E-02	2.66E+09	6.74E+07	2.53E+00		
AVG		2.02E+09	6.03E+07			**Min**
ST DEV		6.53E+08	1.91E+07		**Load (N)**	2.55E-02
					E (Pa)	1.84E+09
					Stress (Pa)	1.74E+07
					Strain	2.43

Sample 4	Load (N)	E (Pa)	Stress (Pa)	% Strain		
1	1.37E-01	5.52E+09	9.53E+07	1.73E+00		
2	8.23E-02	3.10E+09	5.72E+07	1.84E+00		**Average**
3	1.03E-01	2.83E+09	7.12E+07	2.52E+00	**Load (N)**	1.19E-01
4	1.48E-01	3.85E+09	1.03E+08	2.68E+00	**E (Pa)**	3.70E+09
5					**Stress (Pa)**	8.29E+07
6					**Strain**	2.26E+00
7	1.29E-01	3.67E+09	8.98E+07	2.45E+00		
8	1.25E-01	3.40E+09	8.69E+07	2.55E+00		**Max**
9	1.34E-01	3.74E+09	9.33E+07	2.50E+00	**Load (N)**	1.48E-01
10	1.08E-01	3.90E+09	7.48E+07	1.92E+00	**E (Pa)**	5.52E+09
11	1.26E-01	3.76E+09	8.78E+07	2.34E+00	**Stress (Pa)**	9.53E+07
12	1.21E-01	3.92E+09	8.42E+07	2.15E+00	**Strain**	2.68
13	9.77E-02	3.06E+09	6.78E+07	2.22E+00		
AVG		3.70E+09	8.29E+07			**Min**
ST DEV		7.10E+08	1.36E+07		**Load (N)**	8.23E-02
					E (Pa)	2.83E+09
					Stress (Pa)	5.72E+07
					Strain	1.73

Sample 5	Load (N)	E (Pa)	Stress (Pa)	% Strain		
1						
2						**Average**
3	1.36E-01	4.76E+09	8.58E+07	1.80E+00	**Load (N)**	1.38E-01
4	1.17E-01	4.65E+09	7.37E+07	1.58E+00	**E (Pa)**	4.98E+09
5	1.61E-01	5.20E+09	1.01E+08	1.95E+00	**Stress (Pa)**	8.71E+07
6					**Strain**	1.75E+00
7	1.34E-01	5.58E+09	8.43E+07	1.51E+00		
8	1.44E-01	4.69E+09	9.05E+07	1.93E+00		**Max**
9					**Load (N)**	1.61E-01
10					**E (Pa)**	5.58E+09
11					**Stress (Pa)**	1.01E+08
12					**Strain**	1.95
13						
AVVG		4.98E+09	87077792			**Min**
ST DEV		4.03E+08	9985790.4		**Load (N)**	1.17E-01
					E (Pa)	4.65E+09
					Stress (Pa)	7.37E+07
					Strain	1.51